Nanoscale

PAPER

View Article Online
View Journal | View Issue

Cite this: *Nanoscale*, 2025, **17**, 15905

Photothermoelectric effect driven self-powered broadband photodetection in 1T′-$MoTe_2$ with asymmetric electrodes†

Youqi Zhang,‡ Lan Li,‡ Yinuo Zhang,* Yifan Liu, Yunan Lin, Xutao Zhang, Yongqi Hu, Xiaoqiang Sun, Bingyan Ai and Yi Pan *

Photothermoelectric (PTE) detection provides a versatile platform for uncooled ultra-broadband photosensing applications. The responsivity and speed of PTE-based photodetectors can be significantly enhanced by introducing two-dimensional (2D) topological Weyl semimetals owing to their unique tilting Weyl cones, high carrier mobilities, and hot-carrier-assisted transport. However, the requirement of localized illumination and complex device fabrication processes still hinder their broader application. Here, a high-performance 1T′-$MoTe_2$ PTE-based detector with asymmetric electrodes is constructed by employing ultra-high vacuum stencil lithography. The asymmetry is achieved by leveraging differential doping efficiencies at the metal contacts, breaking the mirror symmetry of the Seebeck coefficient profile across the channel. This architecture enables the generation of a self-powered photocurrent even under global illumination conditions. The detector shows a broadband response from 350 to 1200 nm, achieving a responsivity of 8.22 mA W^{-1} and a detectivity of 7.11 × 10^9 Jones. Furthermore, it demonstrates fast response dynamics with a rising time of 15.4 μs and a decay time of 8.4 μs. Our proposed strategy opens up the application of 2D Weyl semimetals in PTE-based photodetectors with the advantage of self-powering, broadband, and fast response.

Received 26th February 2025,
Accepted 3rd June 2025

DOI: 10.1039/d5nr00855g

rsc.li/nanoscale

1. Introduction

The photothermoelectric effect (PTE) is a unique photoresponse mechanism that forms a carrier concentration gradient and temperature gradient in thermoelectric materials by photoexcitation, which induces the Seebeck effect to drive electrical signals. The PTE-based photodetectors exhibit ultra-broadband response at room temperature, especially working in the mid-infrared and terahertz (THz) frequency without the limitation of the bandgap. They offer the advantages of low power consumption and low noise due to their self-powering capability. Thus, PTE-based photodetectors could be widely used in fields such as weak signal detection, broad-band sensing, and infrared imaging. Normally, the asymmetric distribution of temperature and the Seebeck coefficient is induced in mechanical exfoliation of van der Waals (vdW) flakes by local illumination on one of the two electrodes, which is a crucial condition. The exfoliation of vdW thin flakes also suffer from limited area, hindering its application in high-throughput and large-scale photoelectric detection,[1–5] while local illumination is limited by the diffraction limit, restricting its application in sensing and imaging.[2,6–9] Recently, much research efforts have been made in the innovation of device structure to achieve PTE under global illumination, including PN junctions,[10] double-gated devices,[11] asymmetric heat dissipation channels,[12] and localized plasmonic nanostructures.[13] The above strategies suffer from complex device fabrication, external gate voltage modulation, and limited wavelengths from plasmon resonance. Therefore, we propose that introducing asymmetric electrodes into devices is a promissing solution to overcome the above difficulties. Specifically, the PTE effect could be realized by an asymmetric Seebeck coefficient distribution induced by the asymmetric doping at the electrode–material interface. Similarly, PTE-based graphene devices with asymmetric electrodes have achieved highly sensitive and ultrafast THz detection.[14] In terms of obtaining asymmetric electrodes, extensive photolithography process will increase the risk of surface contamination and internal damage of the material, which is unfavourable for attaining an asymmetric Seebeck coefficient through interfacial metal doping. To obtain reliable and high-performance PTE devices,

Center for Spintronics and Quantum Systems, State Key Laboratory for Mechanical Behavior of Materials, Xi'an Jiaotong University, Xi'an 710049, China.
E-mail: ynuozhang@outlook.com, yi.pan@xjtu.edu.cn

†Electronic supplementary information (ESI) available. See DOI: https://doi.org/10.1039/d5nr00855g

‡Contributed equally.

the vaccum stencil lithography method for asymmetric electrode fabrication is needed.

Compared with the traditional bulk thermoelectric materials, the novel 2D thermoelectric materials could further enhance the device performance due to their strong interband coupling, direct band structure, and excellent electrical and thermoelectric properties.[15,16] Notably, two-dimensional topological semimetals like WTe_2 and 1T′-$MoTe_2$ have broad operating bandwidths and ultrahigh carrier mobilities.[17–21] Theoretical studies have shown that type-II Weyl semimetals (WSMs) can generate strong photocurrents at edges, and the thermoelectric anisotropy of the material also facilitates the collection of photocurrents.[22] Furthermore, the large tilting angle of Weyl nodes can reduce the effective mass of photocarriers, thereby enhancing the responsivity (R).[23,24] However, photodetectors based on WSMs typically exhibit suboptimal performance, particularly in terms of response time and detectivity.[25] Thus, the thickness dependency of PTE effects in semimetal-based devices needs further investigation, since suppressed PTE performance has been observed in the atomically thin layer material due to the lack of interfacial asymmetric doping.[26] Addtionally, large-scale 1T′-$MoTe_2$ film synthesis remains a critical challenge for device integration.

In this work, we report a PTE-based photodetector fabricated on 1T′-$MoTe_2$ with asymmetric metal electrodes. A large-scale 1T′-$MoTe_2$ film with controllable thickness was synthesized by a two-step tellurization method *via* chemical vapor deposition (CVD). By utilizing the shadow-mask-assisted stencil lithography in a ultra-high vacuum (UHV) environment, Au and Pd electrodes were successfully deposited on large-scale layered 1T′-$MoTe_2$ films. The obtained asymmetric Seebeck coefficient distribution from interfacial doping of different electrode materials results in a high-performance PTE-based photodetector. The device exhibits a broadband response from ultraviolet to infrared (350–1200 nm), with high responsivity of up to ~8.22 mA W^{-1}, and fast response speeds up to 15.4 μs (rising time) and 8.4 μs (decay time) at 0 V. Our work provides an efficient strategy to achieve high-performance broadband photodetectors based on WSMs.

2. Experimental section

2.1 Epitaxial growth of 1T′-$MoTe_2$ films

To obtain large-scale 1T′-$MoTe_2$ thin films, we adopted a two-step CVD-assisted tellurization method as shown in Fig. 1a. SiO_2 (300 nm)/Si wafers were used as the substrates. Each piece was cut into 3 × 12 mm^2 rectangular shapes to fit the flag type sample holders. A home-built sublimation evaporator with a molybdenum (Mo) wire filament of 150 μm diameter was used for Mo precursor layer deposition, as shown in Fig. S1a.† The saturation vapor pressure temperature of Mo was effectively reduced in an UHV environment (1592 °C to 1822 °C for the pressure range of 10^{-6}–10^{-4} Pa). The deposition of Mo films was achieved *via* direct current (DC) heating of the wire. The thickness of the Mo film can be controlled by changing the evaporation time (1, 5, and 15 min) under a constant power of 16 W. It can be seen from optical microscopy (OM) pictures in Fig. S1b and c† that the thickness of the Mo film changes obviously with an increase of deposition time. To balance the optoelectronic properties and thickness-dependent metal doping effect in materials, the 5 min deposited Mo films exhibiting optimal thickness–performance characteristics were selected for further tellurization. Additionally, the distance between the evaporator and the substrate was 12 mm. During the 35 min tellurization process in CVD, high-purity Te powder (80 mg, 99.99%) and Mo film were positioned at the first and second centers of the dual heating zone tube furnace, and they were separately heated to T_1 (873 K) and T_2 (973 K). The heating process is shown in Fig. S2.† The tellurization of Mo films with different thicknesses enables the control of thickness of the resulting 1T′-$MoTe_2$ film. The typical thicknesses of $MoTe_2$ films obtained by tellurizing Mo films deposited for 5 and 10 minutes as shown in Fig. S3,† are around 20 nm and 40 nm, respectively. This two-step method is beneficial for the growth of continuous, large-area 1T′-$MoTe_2$ films rather than isolated islands. A counterflow of a gas mixture of Ar (90%) and H_2 (10%) at 100 sccm filled the tube, which prevented the Te powder from oxidation and the early transportation of vaporized Te to the Mo film. During the growth period, a forward flow of a gas mixture of Ar (95%) and H_2 (5%) at 50 sccm was introduced. As a matter of fact, we found that the phase composition of the $MoTe_2$ films is strongly dependent on the tellurization time which is shown in Fig. S4.† Specifically, a shorter tellurization time, such as 10 min, favors the formation of 1T′-$MoTe_2$ with a large size due to the relatively low supply of Te at the initial stage, compared with 2H-$MoTe_2$ formed within 30 min of tellurization. Photographs of the multi 2H-$MoTe_2$ and 1T′-$MoTe_2$ devices can be seen in Fig. S5.† As a result, the process enables reliable phase conversion and high-quality film formation suitable for device integration.

2.2 Device fabrication

To achieve the metal doping effect on the obtained 1T′-$MoTe_2$, we need to choose the materials with appropriate work functions from those widely used metal electrodes. Considering the conductivity and stability of these metal electrodes under the air atmosphere, we selected Au and Pd as the electrodes because of their high stability and dramatic work function differences. Since the PTE effect is sensitive to doping, a contaminated surface and damaged material will modify both the electrical properties and PTE performance (*e.g.*, unintentional charge transfer doping from the residue photoresist, radiation damage, and impurity absorption). The conventional photolithography method, which is performed on the surfaces of materials, cannot be used here.[27,28] To eliminate the above issues,[29,30] the electrodes were fabricated using the stencil lithography method in a home-built UHV multi-source physical vapor deposition (PVD) system, which operates at 10^{-5} Pa and effectively protects the material surface from oxidation or extra contamination. As shown in Fig. 1c, shadow masks were

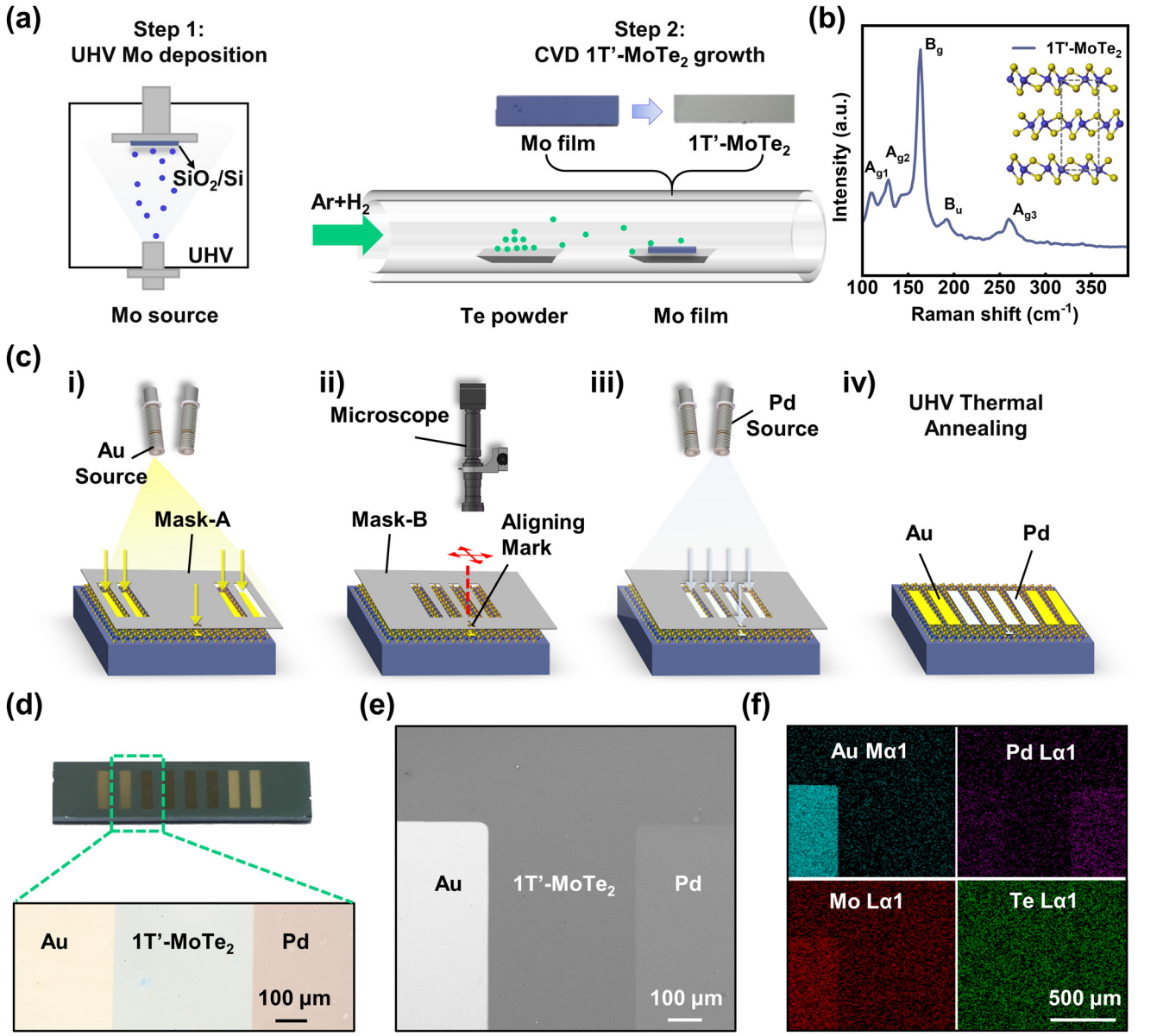

Fig. 1 Au/1T′-$MoTe_2$/Pd PTE-based detector characterization and fabrication. (a) Schematic diagram of 1T′-$MoTe_2$ grown by the two-step method. Step 1: the growth of the Mo film. Step 2: the growth of few-layer 1T′-$MoTe_2$ on a SiO_2/Si substrate through CVD-assisted tellurization. (b) The Raman spectrum of the CVD 1T′-$MoTe_2$ film. (c) Schematic diagram of the device electrode preparation process by the UHV stencil lithography technique. (d) Photograph and optical image of the 1T′-$MoTe_2$ film with Pd electrodes and Au electrodes. (e) SEM image of the device prepared using the process in (c). (f) EDS elemental mapping of Au, Pd, Mo, and Te distribution in the area shown in (e).

designed to achieve electrode patterns. Also, thicknesses were calibrated by using a quartz crystal microbalance (QCM, TMC13, PREAVC). Au and Pd electrodes were deposited by using K-cell evaporators and then thermally annealed for enhanced interfacial contacts. Using this approach, we realized the combination of multiple metal electrodes, like Au–Au, Au–Pd, and Pd–Pd.

2.3 Characterization

The Raman spectra were recorded with a confocal Raman spectrometer (HORIBA) equipped with a 532 nm laser (Renishaw InVia Qontor) at room temperature. The surface structure measurements were performed using a commercial scanning electron microscope (SEM) (MIRA3-LMH, Tyco electronics) operated at 15 kV. The film thickness was characterized by atomic force microscopy (AFM, SPM-9700HT). The electrical and optoelectrical properties of the devices were investigated using a Keithley 2636B (Tektronix). A high-pressure Xe lamp (CME-SL300, Microenerg, wavelength: 300–2500 nm) equipped with bandpass filters was employed as the light source. Ultraviolet (UV: 300–400 nm), visible (VS: 400–780 nm), and infrared (IR: 800–1200 nm) filters were selectively obtained

for the corresponding band. The response speed of our device was evaluated with a trans-impedance amplifier and a digital storage oscilloscope (DSO-X3052A, Agilent). The optical pulses were generated using fiber-coupled lasers (Oaebt OF-20B) with optical power modulation.

3. Results and discussion

3.1 Asymmetric electrodes on large scale 1T′-$MoTe_2$

The phase structure of the as-grown $MoTe_2$ was first identified by Raman spectroscopy, as shown in Fig. 1b. The phase-specific characteristic Raman peaks of A_{g1} (109.1 cm^{-1}), A_{g2} (128.6 cm^{-1}), B_g (163.6 cm^{-1}), B_u (192.7 cm^{-1}) and A_{g3} (260.1 cm^{-1}) vibration modes[31–34] correspond to 1T′-$MoTe_2$, while the sharp peaks reflect the high crystallization of 1T′-$MoTe_2$. To evaluate the morphology of the asymmetric Au/Pd electrodes deposited on the surface of 1T′-$MoTe_2$, optical microscopy (OM) and scanning electron microscopy (SEM) were used for characterization. Fig. 1d shows typical photo and OM images of the as-grown 1T′-$MoTe_2$ with Au and Pd electrodes. It can be seen that the surface of the device is flat and clean, without surface contamination, which benefits from the electrode fabrication method under an UHV environment. The channel area of a single device is about 1 mm^2. Due to the clean interface between the material and the electrode, the devices can exhibit ohmic contacts with both symmetric and asymmetric electrodes. Moreover, as illustrated in Fig. 1e and f, the SEM image and energy dispersive spectrometry (EDS) conducted on the 1T′-$MoTe_2$ device exhibit a uniform element distribution. The observed slight enhancement of the Mo signal in the Au electrode region is attributed to the overlap of characteristic X-ray peaks of Mo and Au as shown in Fig. S6.†

3.2 PTE dominated photoresponse under global illumination

To further explore the device performance with asymmetric electrodes, Fig. 2a illustrates the schematic of the Au/1T′-$MoTe_2$/Pd device for optoelectronic measurement. We defined the direction as positive when the electron transport occurred from the Au to Pd electrode. The transport properties of the Au/1T′-$MoTe_2$/Pd photodetectors were measured under darkness and 648 nm laser illumination with various light power densities at 300 K, as shown in Fig. 2b. The open-circuit voltage (V_{oc}) of 2 mV and short-circuit current (I_{sc}) of 2.14 μA were obtained at P = 44 mW cm^{-2}, which indicate that our device can work at zero bias. It is notable that the direction of the short-circuit current is negative, and the photocurrent exhibited a linear dependence on voltage. Such phenomena can be understood as the result of the photovoltaic effect (PVE)[35–39] and PTE effect. Generally, these two effects can coexist in a photodetector, and they exhibit opposite photocurrent directions. Photodetectors based on the PVE effect separate photocarriers by the built-in electric fields, and I–V curves exhibit rectifying characteristics, while the I–V curve of PTE-based detectors can be linear,[15] as their photoresponse originates from temperature gradients or spatial variations under illumination in combination with differences in the Seebeck coefficient. These mechanisms generally do not influence the linearity of the I–V curve under dark conditions. In our PTE device, the clean interface between the metal electrodes and 1T′-$MoTe_2$, achieved *via* ultra-high vacuum fabrication, facilitates excellent ohmic contact. Consequently, the device demonstrates a linear I–V response consistent with the intrinsic semimetallic nature of 1T′-$MoTe_2$ in Fig. S7.† On the other hand, the direction of the current for photodetectors with the PVE effect is consistent with the work function gradient, as shown in Fig. 2c. The direction of the PVE photocurrent based on the work functions of 1T′-$MoTe_2$ (5.07 eV),[40] Pd (5.69 eV)[41] and Au (5.1 eV)[42] should be positive,[26,43–45] which is contrary to the experimental observation. Therefore, we conclude that the photocurrent is dominated by the PTE effect in our device. To investigate the dynamic behaviour of photogenerated carriers of the Au/1T′-$MoTe_2$/pd device, analysis of the PTE effect is carried out.

Precisely, the Seebeck coefficient is the transport entropy of charge carriers, which is the entropy transferred per unit charge in thermodynamics, and provides a quantitative relationship between the S and the carrier density n.[46] The Seebeck coefficient can be defined as follows:[47]

$$S = -\frac{\pi^2 {k_b}^2 T}{3e} \frac{1}{G} \frac{dG}{dE_{E=E_f}} \quad (1)$$

where k_b is the Boltzmann constant, e is the single electron charge, T is the temperature, G is the conductance, and E_f is the Fermi energy. The conductivity G is proportional to the charge density n and the mobility μ. Additionally, based on the quantitative relationship between the Seebeck coefficient and the Fermi level in semiconductors,[44] the Seebeck coefficient is related to metal doping. Therefore, Fig. 2d shows that the Seebeck coefficient of a P^- type semiconductor is larger than that of P^+ type and undoped semiconductors.[48] The existence of Au and Pd leads to charge doping between the interface of electrodes and 1T′-$MoTe_2$. Also, more doping happened on the interface of 1T′-$MoTe_2$/Pd, due to the larger difference in the work function. Consequently, it can be inferred that the Seebeck coefficient $S(x)$ in 1T′-$MoTe_2$ exhibits a dependence on the selected position x on the channel without bias as shown in Fig. 2e. Due to the experimental challenges in directly mapping the Seebeck coefficient, we instead inferred its spatial asymmetry through elemental gradient analysis at the metal–$MoTe_2$ interfaces, which supports the proposed PTE mechanism, as shown in Fig. S8.†

The potential gradient generated by the PTE effect can be formulated as follows:[14]

$$\nabla V(x) = -S \nabla T(x) \quad (2)$$

where S is the Seebeck coefficient and ∇T is the temperature gradient. Fig. 2f shows the quantitative relationship between PTE-dominated photo response and the temperature gradient ∇T and the Seebeck coefficient S. It is obvious that some of the photons can be converted into electronic heat by the material

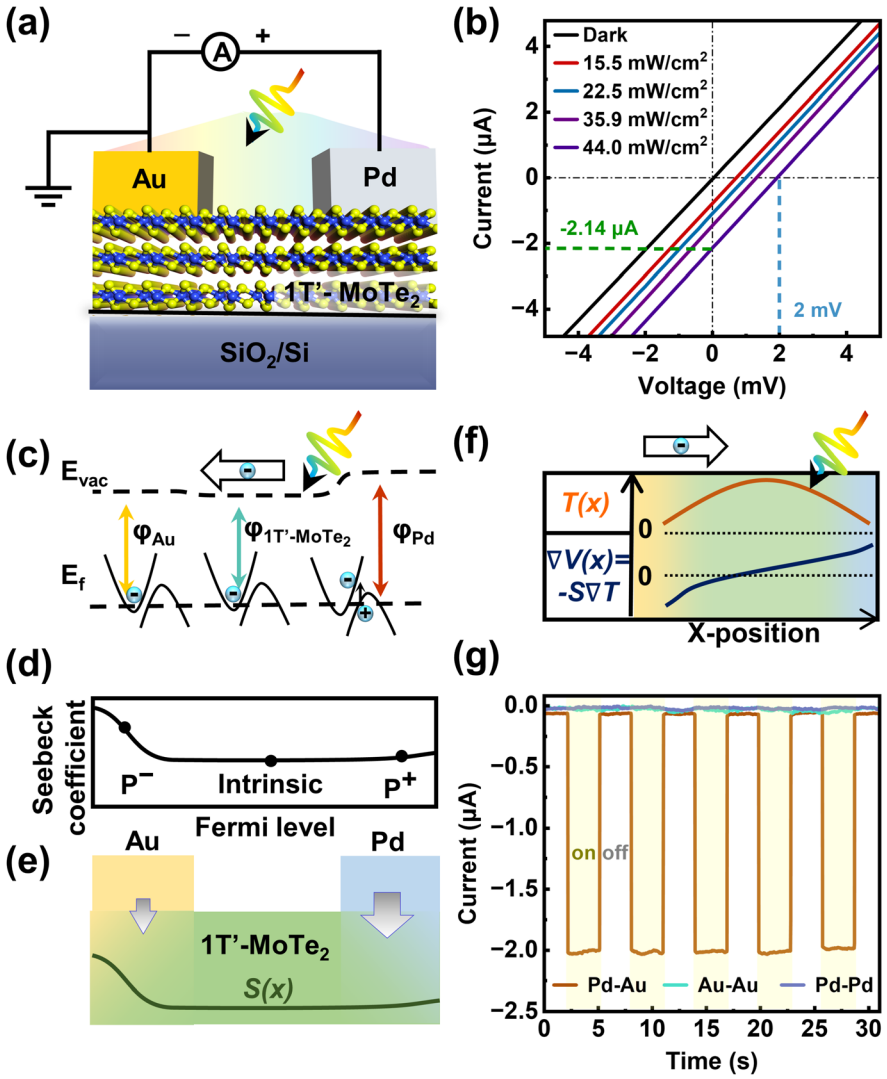

Fig. 2 PTE mechanism analysis of the Au/1T′-$MoTe_2$/Pd detector. (a) Au/1T′-$MoTe_2$/Pd device structure and external circuit. (b) *I*–*V* curves of the detector under varying power intensities. (c) The energy band diagram of the device and the schematic of its PVE mechanism under illumination. (d and e) Schematic diagrams of the electrostatic doping and Seebeck coefficient distribution in the detector with asymmetric electrodes, respectively. (f) Schematic diagram of PTE response mechanism under global illumination. (g) Comparison of the time-dependent photoresponse to pulsed white light illumination of the devices with Pd–Au, Au–Au, and Pd–Pd electrode pairs at V_{bias} = 0.

under illumination. Due to the poor thermal conductivity of the SiO_2/Si substrate and the metal electrodes, it will result in a gradient profile of the electron temperature $T(x)$ along the channel. However, $\nabla T(x)$ tends to be uniformly distributed along the channel under global illumination owing to the similar thermal conductivity of Pd and Au electrodes. Moreover, the asymmetric distribution of the Seebeck coefficient along the channel determines the photovoltage generated by the PTE effect, since the total voltage is the integral of $\nabla V(x)$ along the *x*-direction. Therefore, negative photocurrent (from Au to Pd) will be obtained, which is consistent with our experiment. When a bias is applied to the device, the built-in electric field and the Seebeck coefficient profile will change accordingly, which leads to an increase or decrease in the photocurrent. The thickness of 1T′-$MoTe_2$ is a key factor to realizing the PTE effect caused by asymmetrical metal doping, since excessively thin films hinder thermal gradient formation and carrier modulation, limiting the photothermoelectric response. In deed, our previous work suggests that the PVE effect is neglectable when the CVD-grown 1T′-$MoTe_2$ film has the thickness of 3–4 monolayer.[26] Next, the photoresponse characteristics of the Au/1T′-$MoTe_2$/Pd, Au/1T′-$MoTe_2$/Au, and Pd/1T′-$MoTe_2$/Pd devices were measured without applying voltage. Fig. 2g shows plots of the *I*–*t* curves of these devices under white illumination. It is notable that only the device with asymmetric electrodes shows obvious photocurrent at 0 bias, while Au/1T′-$MoTe_2$/Au and Pd/1T′-$MoTe_2$/Pd devices show neglectable photocurrent. Also, *I*–*V* curves shown in Fig. S7† confirm the absence of self-powering ability for devices with symmetric electrode materials. Based on these

results, it is clear that the asymmetric electrode in the 1T′-$MoTe_2$ device is crucial for achieving high performance of broadband and self-power under global illumination.

3.3 Device performance: self-power, broadband, and fast response

To further evaluate the device performance, we investigated the optoelectronic performance of our photodetector using a Xe lamp and fiber lasers, which could provide constant or pulsed illumination to the device. Fig. 3a shows the *I*–*V* curves of the device under darkness and illumination with various wavelengths obtained by the VS, UV, and IR filters at 300 K. It demonstrates that the device exhibits broadband photoresponse from UV to IR. Fig. 3b illustrates the fitting relationship of the photocurrent with the optical power according to the equation: $I_{ph} \propto AP^{\alpha}$, where P is the optical power intensity and α is a constant to be fitted. α values for UV, VS, and IR were 0.663, 0.642, and 0.641, respectively. The dependence of I_{ph} on P at V = 0 V exhibits a typical sublinear relationship, indicating that the PTE effect exists in our photodetectors.[49] Meanwhile, Fig. 3c depicts the time-resolved photoresponse of the devices at 0 V, demonstrating a stable and fast response in a wide band range from UV to IR, which also indicates the self-power capability of the device in broadband. Such a broadband photoresponse is attributed to the gapless WSMs type band structure of 1T′-$MoTe_2$, which enables detection even for far-infrared and THz regimes.[3] Based on the obtained result, the distribution of asymmetric Seebeck coefficients still exists during illumination. The performance of the devices was evaluated under varying power densities. As shown in Fig. 3d, a rapid and stable photoresponse was observed at every given wavelength, indicating high stability and repeatability of our photodetector. With the increase of optical power, the photocurrent tends to stabilize at P = 46.3 mW cm^{-2} as shown in Fig. S9,† which can be attributed to a reduced potential gradient in the device, which is caused by the limited temperature gradient of the material under illumination with high optical power.[8,50] Consequently, such results suggest that the device can operate as a self-powered broadband photodetector.

We have calculated photoresponsivity (R) and specific detectivity (D^*) according to the following formulas:

$$R = \frac{I_{ph}}{PS} \tag{3}$$

$$D^{\star} = \frac{R\sqrt{S}}{(2eI_{dark})^{1/2}} \tag{4}$$

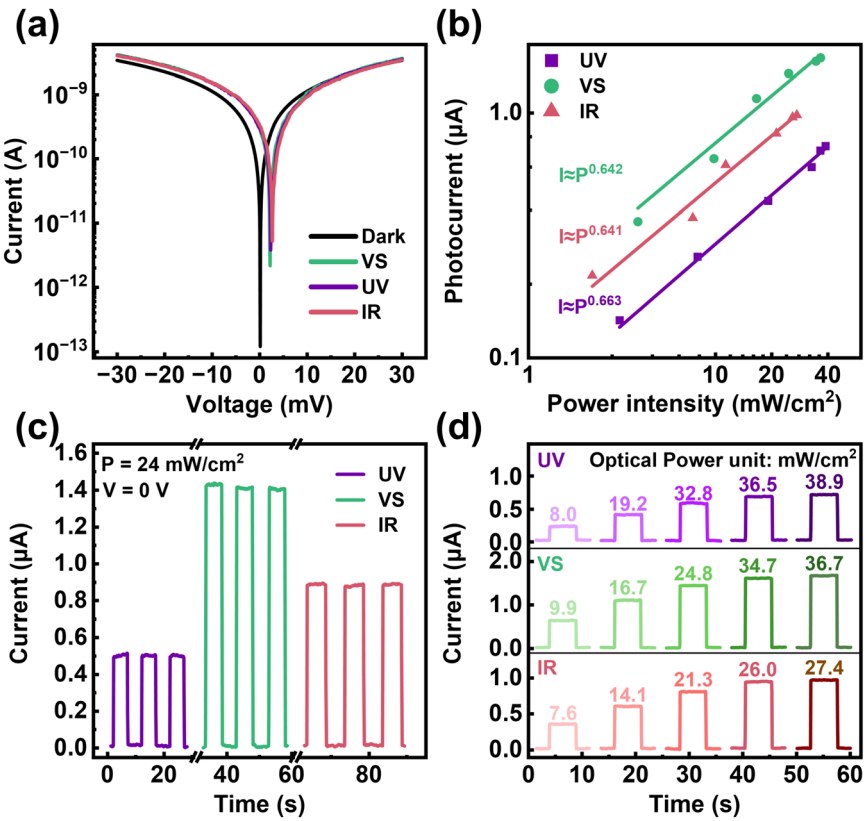

Fig. 3 The broadband characteristic and the durability of the Pd/1T′-$MoTe_2$/Au PTE-based detector. (a) *I*–*V* curves obtained in the dark and under the illumination of constant light power intensity with bandpass filters for IR (red), VS (blue), and UV (purple) light. (b) The corresponding fitting curve of photocurrent *versus* power intensity. (c and d) Time-dependent photoresponse under pulsed light with different spectral bands at the same and various light intensities (unit: mW cm^{-2}).

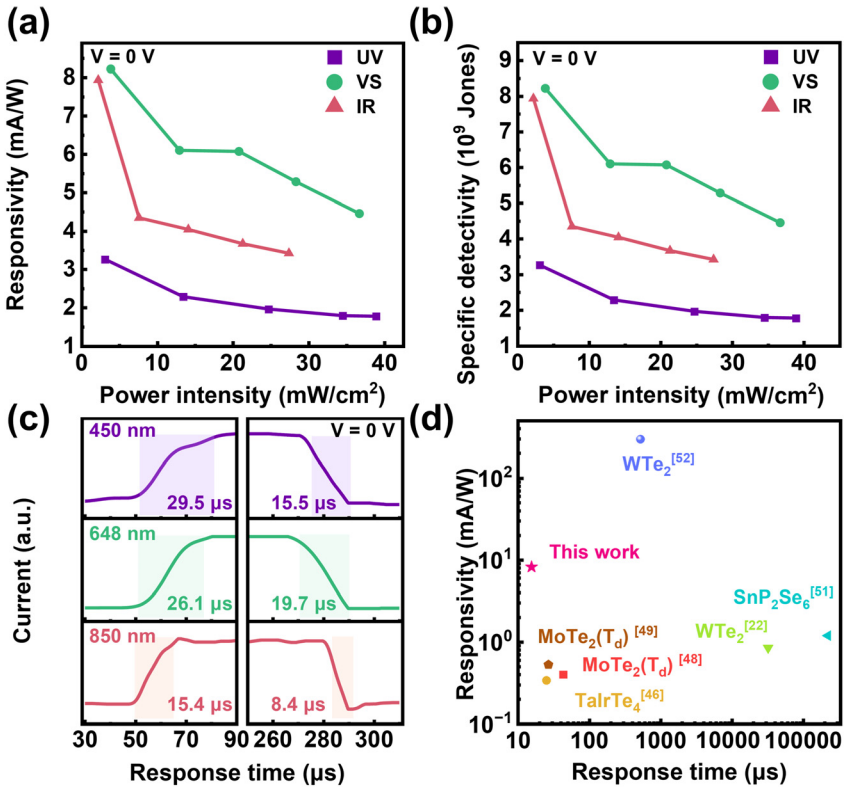

Fig. 4 The key parameters of the Au/1T′-$MoTe_2$/Pd PTE-based detector. (a) The responsivity of the detector as a function of power intensity under light with different spectral bands. (b) The specific detectivity of the detector as a function of power intensity under light with different spectral bands. (c) Rising and decay time of the detector obtained under pulsed laser beam illumination of different wavelengths (450, 648, 850 nm). (d) Comparison of the responsivity and response time of our device and other WSMs devices.

where I_{ph} is the photocurrent, S is the effective area of the device, P is the optical power density, e is the single electron charge, I_{dark} is the dark current, and R is the responsivity.[51] Fig. 4a and b show the evolution of D^* and R in response to P at every given wavelength. The device achieved the maximum R of 8.22 mA W^{-1} at a wavelength of 648 nm at 0 V. The values of D^* for our device reach 2.82×10^9 Jones, 7.11×10^9 Jones, and 6.87×10^9 Jones corresponding to UV, VS, and IR illumination, respectively. It is worth mentioning that when dark current is used to calculate the detectivity of photodetectors, there will be an overestimated D^*. Therefore, we also investigated the noise-equivalent power (NEP) of the device to more accurately determine D^*(see note 1 in the ESI†). Furthermore, the response speed of the photodetector at wavelengths of 450 nm, 648 nm, and 850 nm was also investigated. Fig. 4c shows the time-resolved photocurrent at V = 0 V by choosing a pulsed laser as the irradiation source. The response speed measurement reveals that the highest value is 15.4 μs for rising and 8.4 μs for decaying under illumination of 850 nm, confirming the rapid separation of photogenerated electrons and holes. The actual response speed may be higher than the obtained result due to the equipment limitation. Such rapid responses can be attributed to the shorter transient lifetime of photocarriers due to rapid electron–electron scattering in the absence of a bandgap.[52] Additionally, the built-in potential plays a crucial role in accelerating the separation of the photocarriers. More importantly, there is no obvious degradation of photodetector performance observed even after 12 months of exposure to air, suggesting great durability of the device, as shown in Fig. S11.†

To compare the performance of our devices with published research, Fig. 4d shows the comparison of the responsivity of our device with other type-II WSM devices induced by local illumination and the PTE effect.[25,53–60] The Au/1T′-$MoTe_2$/Pd photodetector exhibits an ultrafast response time of 15.4/8.4 μs and a response band ranging from UV to IR compared with that of reported photodetectors. Our device also has merits in the value of D^* as shown in Fig. S12† among these detectors, which confirms that the PTE effect caused by metal doping offers distinct advantages in obtaining high performance photodetectors. Our work demonstrates a novel design concept for the fabrication of high-performance, broadband photodetectors based on Weyl semimetals.

4. Conclusion

We have synthesized large-scale two-dimensional 1T′-$MoTe_2$ on a Si/SiO_2 substrate using the two-step CVD tellurization method. Asymmetric Au and Pd electrodes were designed to

achieve the PTE-dominated photoresponse under global illumination. Au/1T′-$MoTe_2$/Pd devices with ultraclean interfaces were fabricated using a stencil lithography method in UHV. The detector exhibits the capability of self-powered detection and a broadband photoresponse range from 350 nm to 1200 nm. The device shows a high responsivity of 8.22 mA W^{-1} and a large specific detectivity of 7.11×10^9 Jones. Meanwhile, the device features response times up to 15.4 μs (rising time) and 8.4 μs (decaytime). Such a high performance benefits from the special electrode fabrication method in an UHV environment, which effectively promotes the asymmetric Seebeck coefficient distribution along the channel, leading to a significant PTE effect under global illumination. These results shed light on the potential applications of 2D layered Weyl semimetal materials in the application of optoelectronic devices with a broadband, self-powered, and fast response.

Author contributions

Yi Pan conceived and supervised the experiments. Youqi Zhang conducted the sample growth, device fabrication and data collection with the assistance of Yifan Liu and Yunan Lin. Lan Li conducted data analysis and explanation. Xiaoqiang Sun conducted the AFM measurement. Bingyan Ai conducted SEM and EDS measurements. Yinuo Zhang and Yi Pan validated the results. Youqi Zhang, Lan Li and Yi Pan wrote the manuscript with the input of all authors.

Data availability

The data supporting this article have been included within the article and its ESI.†

Conflicts of interest

There are no conflicts to declare.

Acknowledgements

This work was financially supported by the National Key Research and Development Program of China (Grant no. 2022YFA1204100) and the National Natural Science Foundation of China (Grant no. 12074302). We thank the Instrumental Analysis Center of Xi'an Jiaotong University for their assistance with the Raman measurement.

References

1 J. Lai, X. Liu, J. Ma, Q. Wang, K. Zhang, X. Ren, Y. Liu, Q. Gu, X. Zhuo, W. Lu, Y. Wu, Y. Li, J. Feng, S. Zhou, J.-H. Chen and D. Sun, *Adv. Mater.*, 2018, **30**, 1707152.
2 Q. Yang, X. Wang, Z. He, Y. Chen, S. Li, H. Chen and S. Wu, *Adv. Sci.*, 2023, **10**, 2205609.
3 Q. Wang, J. Zheng, Y. He, J. Cao, X. Liu, M. Wang, J. Ma, J. Lai, H. Lu, S. Jia, D. Yan, Y. Shi, J. Duan, J. Han, W. Xiao, J.-H. Chen, K. Sun, Y. Yao and D. Sun, *Nat. Commun.*, 2019, **10**, 5736.
4 J. Ma, Q. Gu, Y. Liu, J. Lai, P. Yu, X. Zhuo, Z. Liu, J.-H. Chen, J. Feng and D. Sun, *Nat. Mater.*, 2019, **18**, 476–481.
5 M. P. Singh, J. Kiemle, I. Ozdemir, P. Zimmermann, T. Taniguchi, K. Watanabe, M. Burghard, O. Üzengi Aktürk, C. Kastl and A. W. Holleitner, *2D Mater.*, 2022, **9**, 011002.
6 W. Deng, C. Wang, M. Dai, F. Wang, J. Han, F. Sun, Q. J. Wang and Y. Zhang, *Appl. Phys. Lett.*, 2022, **121**, 112105.
7 Y. Wang, Y. Niu, M. Chen, J. Wen, W. Wu, Y. Jin, D. Wu and Z. Zhao, *ACS Photonics*, 2019, **6**, 895–903.
8 W. Dai, W. Liu, J. Yang, C. Xu, A. Alabastri, C. Liu, P. Nordlander, Z. Guan and H. Xu, *Light: Sci. Appl.*, 2020, **9**, 120.
9 G. Li, S. Yin, C. Tan, L. Chen, M. Yu, L. Li and F. Yan, *Adv. Funct. Mater.*, 2021, **31**, 2104787.
10 S. Castilla, B. Terrés, M. Autore, L. Viti, J. Li, A. Y. Nikitin, I. Vangelidis, K. Watanabe, T. Taniguchi, E. Lidorikis, M. S. Vitiello, R. Hillenbrand, K.-J. Tielrooij and F. H. L. Koppens, *Nano Lett.*, 2019, **19**, 2765–2773.
11 D. J. Groenendijk, M. Buscema, G. A. Steele, S. Michaelis de Vasconcellos, R. Bratschitsch, H. S. J. van der Zant and A. Castellanos-Gomez, *Nano Lett.*, 2014, **14**, 5846–5852.
12 M. Dai, C. Wang, M. Ye, S. Zhu, S. Han, F. Sun, W. Chen, Y. Jin, Y. Chua and Q. J. Wang, *ACS Nano*, 2022, **16**, 295–305.
13 V. Shautsova, T. Sidiropoulos, X. Xiao, N. A. Güsken, N. C. G. Black, A. M. Gilbertson, V. Giannini, S. A. Maier, L. F. Cohen and R. F. Oulton, *Nat. Commun.*, 2018, **9**, 5190.
14 X. Cai, A. B. Sushkov, R. J. Suess, M. M. Jadidi, G. S. Jenkins, L. O. Nyakiti, R. L. Myers-Ward, S. Li, J. Yan, D. K. Gaskill, T. E. Murphy, H. D. Drew and M. S. Fuhrer, *Nat. Nanotechnol.*, 2014, **9**, 814–819.
15 M. Dai, X. Zhang and Q. J. Wang, *Adv. Funct. Mater.*, 2024, **34**, 2312872.
16 X. Lu, L. Sun, P. Jiang and X. Bao, *Adv. Mater.*, 2019, **31**, 1902044.
17 A. A. Soluyanov, D. Gresch, Z. Wang, Q. Wu, M. Troyer, X. Dai and B. A. Bernevig, *Nature*, 2015, **527**, 495–498.
18 J. Jiang, Z. K. Liu, Y. Sun, H. F. Yang, C. R. Rajamathi, Y. P. Qi, L. X. Yang, C. Chen, H. Peng, C. C. Hwang, S. Z. Sun, S. K. Mo, I. Vobornik, J. Fujii, S. S. P. Parkin, C. Felser, B. H. Yan and Y. L. Chen, *Nat. Commun.*, 2017, **8**, 13973.
19 L. Zeng, D. Wu, J. Jie, X. Ren, X. Hu, S. P. Lau, Y. Chai and Y. H. Tsang, *Adv. Mater.*, 2020, **32**, 2004412.
20 D. Wu, Z. Mo, X. Li, X. Ren, Z. Shi, X. Li, L. Zhang, X. Yu, H. Peng, L. Zeng and C.-X. Shan, *Appl. Phys. Rev.*, 2024, **11**, 041401.

21 L. Zeng, W. Han, X. Ren, X. Li, D. Wu, S. Liu, H. Wang, S. P. Lau, Y. H. Tsang, C.-X. Shan and J. Jie, *Nano Lett.*, 2023, **23**, 8241–8248.
22 Y.-X. Wang, X.-Y. Zhang, C. Li, X. Yao, R. Duan, T. K. M. Graham, Z. Liu, F. Tafti, D. Broido, Y. Ran and B. B. Zhou, *Nat. Phys.*, 2023, **19**, 507–514.
23 J. Zhang, T. Zhang, L. Yan, C. Zhu, W. Shen, C. Hu, H. Lei, H. Luo, D. Zhang, F. Liu, Z. Liu, J. Tong, L. Zhou, P. Yu and G. Yang, *Adv. Mater.*, 2022, **34**, 2204621.
24 C.-K. Chan, N. H. Lindner, G. Refael and P. A. Lee, *Phys. Rev. B*, 2017, **95**, 041104.
25 Y. Feng, Y. Zhang, Y. Zhang, X. Miao, Y. Lin, T. Min and Y. Pan, *ACS Appl. Opt. Mater.*, 2024, **2**, 333–340.
26 J. Mao, Y. Zhang, Y. Zhang, Y. Lin, Y. Feng, Y. Hu, M. Shafa and Y. Pan, *ACS Appl. Mater. Interfaces*, 2023, **15**, 28267–28276.
27 Y. Zhang, H. Yu, L. Wang, X. Wu, J. He, W. Huang, C. Ouyang, D. Chen and B. E. Keshta, *Adv. Colloid Interface Sci.*, 2024, **329**, 103197.
28 S. Zhang, R. Chen, D. Kong, Y. Chen, W. Liu, D. Jiang, W. Zhao, C. Chang, Y. Yang, Y. Liu and D. Wei, *Nat. Nanotechnol.*, 2024, **19**, 1323–1332.
29 X. Wang, Y. Hu, S. Y. Kim, R. Addou, K. Cho and R. M. Wallace, *ACS Nano*, 2023, **17**, 20353–20365.
30 G. Kwon, H.-S. Kim, K. Jeong, M. Kim, G. H. Nam, H. Park, K. Yoo and M.-H. Cho, *Small Methods*, 2023, **7**, 2300376.
31 D. Wu, C. Guo, L. Zeng, X. Ren, Z. Shi, L. Wen, Q. Chen, M. Zhang, X. J. Li, C.-X. Shan and J. Jie, *Light: Sci. Appl.*, 2023, **12**, 5.
32 J. C. Park, S. J. Yun, H. Kim, J. H. Park, S. H. Chae, S. J. An, J. G. Kim, S. M. Kim, K. K. Kim and Y. H. Lee, *ACS Nano*, 2015, **9**, 6548–6554.
33 D. H. Keum, S. Cho, J. H. Kim, D.-H. Choe, H.-J. Sung, M. Kan, H. Kang, J.-Y. Hwang, S. W. Kim, H. Yang, K. J. Chang and Y. H. Lee, *Nat. Phys.*, 2015, **11**, 482–486.
34 M. Kan, H. G. Nam, Y. H. Lee and Q. Sun, *Phys. Chem. Chem. Phys.*, 2015, **17**, 14866–14871.
35 K. Xu, Z. Zhao, X. Wu and W. Zhu, *2D Mater.*, 2020, **7**, 025035.
36 Y. Xiao, S. He, X. Fan, Y.-A. Du, Y. Li, L. Zhao and L. Gao, *J. Alloys Compd.*, 2024, **1006**, 176358.
37 M. F. Khan, F. Ahmed, S. Rehman, I. Akhtar, M. A. Rehman, P. A. Shinde, K. Khan, D.-k. Kim, J. Eom, H. Lipsanen and Z. Sun, *Nanoscale*, 2020, **12**, 21280–21290.
38 A. K. Mia, M. Meyyappan and P. K. Giri, *Nanoscale*, 2024, **16**, 8583–8596.
39 S. Aftab, M. W. Iqbal, A. M. Afzal, M. F. Khan, G. Hussain, H. S. Waheed and M. A. Kamran, *RSC Adv.*, 2019, **9**, 10017–10023.
40 S. Zhang, Y. Wu, F. Gao, H. Shang, J. Zhang, Z. Li, Y. Fu and P. Hu, *Adv. Funct. Mater.*, 2022, **32**, 2205299.
41 P. Li, W. Qi and K. Tang, *Chin. J. Phys.*, 2022, **78**, 57–71.
42 C. M. Smyth, R. Addou, C. L. Hinkle and R. M. Wallace, *J. Phys. Chem. C*, 2019, **123**, 23919–23930.
43 N. Guo, W. Hu, T. Jiang, F. Gong, W. Luo, W. Qiu, P. Wang, L. Liu, S. Wu, L. Liao, X. Chen and W. Lu, *Nanoscale*, 2016, **8**, 16065–16072.
44 G. Buchs, S. Bagiante and G. A. Steele, *Nat. Commun.*, 2014, **5**, 4987.
45 K. J. Tielrooij, L. Piatkowski, M. Massicotte, A. Woessner, Q. Ma, Y. Lee, K. S. Myhro, C. N. Lau, P. Jarillo-Herrero, N. F. van Hulst and F. H. L. Koppens, *Nat. Nanotechnol.*, 2015, **10**, 437–443.
46 Y. M. Zuev, W. Chang and P. Kim, *Phys. Rev. Lett.*, 2009, **102**, 096807.
47 X. Xu, N. M. Gabor, J. S. Alden, A. M. van der Zande and P. L. McEuen, *Nano Lett.*, 2010, **10**, 562–566.
48 J. C. W. Song, M. S. Rudner, C. M. Marcus and L. S. Levitov, *Nano Lett.*, 2011, **11**, 4688–4692.
49 E. Linardy, M. Trushin, K. Watanabe, T. Taniguchi and G. Eda, *Adv. Mater.*, 2020, **32**, 2001543.
50 W. Guo, Z. Dong, Y. Xu, C. Liu, D. Wei, L. Zhang, X. Shi, C. Guo, H. Xu, G. Chen, L. Wang, K. Zhang, X. Chen and W. Lu, *Adv. Sci.*, 2020, **7**, 1902699.
51 R. K. Ulaganathan, Y.-Y. Lu, C.-J. Kuo, S. R. Tamalampudi, R. Sankar, K. M. Boopathi, A. Anand, K. Yadav, R. J. Mathew, C.-R. Liu, F. C. Chou and Y.-T. Chen, *Nanoscale*, 2016, **8**, 2284–2292.
52 D. Sun, G. Aivazian, A. M. Jones, J. S. Ross, W. Yao, D. Cobden and X. Xu, *Nat. Nanotechnol.*, 2012, **7**, 114–118.
53 L. Zhang, X. Han, P. Wen, S. Zhang, Z. Zheng, J. Li and W. Gao, *ACS Appl. Nano Mater.*, 2022, **5**, 6523–6531.
54 J. Lai, Y. Liu, J. Ma, X. Zhuo, Y. Peng, W. Lu, Z. Liu, J. Chen and D. Sun, *ACS Nano*, 2018, **12**, 4055–4061.
55 S. Chi, Z. Li, Y. Xie, Y. Zhao, Z. Wang, L. Li, H. Yu, G. Wang, H. Weng, H. Zhang and J. Wang, *Adv. Mater.*, 2018, **30**, 1801372.
56 J. Lai, X. Liu, J. Ma, Q. Wang, K. Zhang, X. Ren, Y. Liu, Q. Gu, X. Zhuo, W. Lu, Y. Wu, Y. Li, J. Feng, S. Zhou, J. H. Chen and D. Sun, *Adv. Mater.*, 2018, **30**, 1707152.
57 Q. Yang, X. Wang, Z. He, Y. Chen, S. Li, H. Chen and S. Wu, *Adv. Sci.*, 2023, **10**, 2205609.
58 J. Wang, H. Wang, Q. Chen, L. Qi, Z. Zheng, N. Huo, W. Gao, X. Wang and J. Li, *Appl. Phys. Lett.*, 2022, **121**, 103502.
59 B. X. Zhu, C. Y. Zhu, J. K. Qin, W. He, L. Q. Yue, P. Y. Huang, D. Li, R. Y. Sun, S. Ye, Y. Du, J. H. Sui, M. Y. Li, J. Mao, L. Zhen and C. Y. Xu, *InfoMat*, 2024, **6**, 12600.
60 S. Verma, R. Yadav, A. Pandey, M. Kaur and S. Husale, *Sci. Rep.*, 2023, **13**, 197.